Radiology

In Vivo ^{35}Cl MR Imaging in Humans: A Feasibility Study[1]

Armin M. Nagel, Dr Rer Nat
Frank Lehmann-Horn, MD
Marc-André Weber, MD
Karin Jurkat-Rott, MD
Maya B. Wolf, MD
Alexander Radbruch, MD, JD
Reiner Umathum, Dr Rer Nat
Wolfhard Semmler, Dr Rer Nat, Dr Med

Purpose: To implement chlorine 35 (^{35}Cl) magnetic resonance (MR) at a 7-T whole-body MR system and evaluate its feasibility for imaging humans.

Materials and Methods: All examinations were performed with ethical review board approval; written informed consent was obtained from all volunteers. Seven examinations each of brain and muscle in healthy volunteers and four examinations of patients were performed. Two patients with histologically confirmed glioblastoma multiforme underwent brain imaging. ^{35}Cl MR and ^{35}Cl inversion-recovery (IR) MR were performed. Two patients with genetically confirmed hypokalemic periodic paralysis underwent calf muscle imaging. Seven multiecho sequences (acquisition time, 5 minutes; voxel dimension, 11 mm^3) were applied to determine transverse relaxation time as affected by magnetic field heterogeneity (T2*) and chlorine concentration. ^{35}Cl and sodium 23 (^{23}Na) MR were conducted with a 7-T whole-body MR system. ^{35}Cl longitudinal relaxation time (T1) and T2* of healthy human brain and muscle were determined with a three-dimensional density-adapted–projection reconstruction technique to achieve short echo times and high signal-to-noise ratio (SNR) efficiency. A nonlinear least squares routine and mono- (T1) and biexponential (T2*) models were used for curve fitting.

Results: Phantom imaging revealed 15-fold lower SNR and much shorter relaxation times for ^{35}Cl than ^{23}Na. In vivo T2* was biexponential and extremely short. Monoexponential fits of T1 revealed 9.2 and 4.0 milliseconds ± 0.7 (standard deviation) for brain and muscle, respectively. In glioblastoma tissue, increased Cl$^-$ concentrations and increased Cl$^-$ IR signal intensities were detected. Voxel dimension and acquisition time, respectively, were 6 mm^3 and 9 minutes 45 seconds (^{35}Cl MR) and 10 mm^3 and 10 minutes (^{35}Cl IR MR). In patients with hypokalemic periodic paralysis versus healthy volunteers, Cl$^-$ and Na$^+$ concentrations were increased. Cl$^-$ concentration of muscle could be determined (voxel size, 11 mm^3; total acquisition time, 35 minutes).

Conclusion: MR at 7 T enables in vivo imaging of ^{35}Cl in human brain and muscle in clinically feasible acquisition times (10–35 minutes) and voxel volumes (0.2–1.3 cm^3). Pathophysiological changes of Cl$^-$ homeostasis due to cancer or muscular ion channel disease can be visualized.

© RSNA, 2014

Online supplemental material is available for this article.

The high concentration gradients across the cell membranes for sodium (Na$^+$), potassium (K$^+$), and chloride (Cl$^-$) ions are the physiologic basis for the respective processes of excitation and inhibition of neurons and heart and muscle cells. The membrane potential of cells can be calculated with the Goldman-Hodgkin-Katz equation by using the intra- and extracellular Na$^+$, K$^+$, and Cl$^-$ concentrations weighted by the membrane conductivity for each of these ions (1,2). While extracellular concentrations are tightly regulated and can easily be measured by means of laboratory analysis of blood samples, methods for measuring cellular Na$^+$, K$^+$, and Cl$^-$ concentrations in vivo are highly desirable and might provide insights into pathophysiological processes in several diseases.

Magnetic resonance (MR) imaging can help to provide the necessary data, since Na$^+$, K$^+$, and Cl$^-$ exhibit isotopes sensitive for MR imaging (sodium 23 [^{23}Na], chlorine 35 [^{35}Cl], and potassium 39 [^{39}K]). Each of these isotopes has a high natural abundance: 100% (^{23}Na), 75.8% (^{35}Cl), and 93.3% (^{39}K). Compared with hydrogen 1 (^{1}H), however, their concentrations are lower by approximately three orders of magnitude in vivo. In addition, their MR imaging sensitivity is significantly lower than that of ^{1}H, rendering their visualization

by means of MR imaging very challenging. Nevertheless, ^{23}Na MR imaging has become a valuable and established tool in clinical research (3–5). Furthermore, the feasibility of ^{39}K MR imaging of human muscle (6) and brain (6,7) in vivo has recently been demonstrated with 7-T (6) and 9.4-T (7) whole-body MR systems. Although ^{35}Cl exhibits even lower MR imaging sensitivity than ^{23}Na (8) and only slightly higher MR imaging sensitivity than ^{39}K, imaging of ^{35}Cl could be an important advance. ^{35}Cl is *the* important anion that is involved in many fundamental physiological processes, such as the inhibition of muscular (9) and neuronal cells (10). Also, it is involved in cell volume regulation (11) and cell migration in cancer (12,13). Skeletal muscle cells, for instance, exhibit a very high Cl$^-$ conductance, which makes up approximately 80% of the total membrane conductance at rest (14). Therefore, it follows that the Goldman-Hodgkin-Katz equation can be approximated by the Nernst equation:

$$U = -61 \text{ mV } \ln\left(\frac{[\text{Cl}]_{\text{int}}}{[\text{Cl}]_{\text{ext}}}\right). \quad (1)$$

The inherent advantage of the Nernst equation is that only intra- ([Cl]$_{\text{int}}$) and extracellular ([Cl]$_{\text{ext}}$) Cl$^-$ concentrations are required to calculate the resting membrane potential *(U)* of muscle cells. In various muscle diseases (eg, periodic paralyses [14]), the resting membrane potential is reduced. Therefore, the purpose of this work was to implement ^{35}Cl MR imaging with a 7-T whole-body MR imaging system and to evaluate its feasibility for imaging of humans.

Materials and Methods

All examinations were performed with ethical review board approval of Heidelberg University (Heidelberg, Germany). Written informed consent was obtained from all volunteers. In total, 14 healthy volunteers (four female subjects, 10 male subjects; mean age, 42 years ± 20 [standard deviation]) were examined. Three healthy volunteers aged 22, 22, and 24 years old were

examined to determine the longitudinal relaxation time (T1) of brain tissue; three volunteers aged 20, 37, and 67 years old were examined to determine the transverse relaxation time as affected by magnetic field heterogeneity (T2*) of brain tissue; and one volunteer aged 67 years old was examined to test the ^{35}Cl MR imaging protocol. Four healthy volunteers aged 19, 43, 47, and 73 years old underwent a muscle examination to determine the Cl$^-$ concentration and the T2*, and three healthy volunteers aged 25, 50, and 68 years old were examined to determine T1. In addition, two female patients who were 67 and 72 years old and had histopathologically confirmed glioblastoma multiforme and two female patients who were 28 and 44 years old and had genetically confirmed hypokalemic periodic paralysis (harboring the L-type calcium-channel mutation R1239H [15]) underwent brain and calf muscle examinations, respectively.

Advances in Knowledge

- MR imaging of ^{35}Cl in humans can be accomplished within clinically acceptable measurement times (10–35 minutes) and voxel dimensions of 6 mm^3 and 11 mm^3 for whole brain and calf muscle imaging, respectively.

- Transverse relaxation time as affected by magnetic field heterogeneity (T2*) of ^{35}Cl is extremely short (eg, fast component of healthy muscle tissue, T2*$_f$, < 0.4 millisecond).

- Pathophysiological changes of the Cl$^-$ homeostasis due to glioblastoma or muscular ion channel disease can be visualized by using ^{35}Cl MR imaging.

The study was conducted from September 11, 2011, until January 17, 2013. Parts of this work were presented at annual meetings of the International Society of Magnetic Resonance in Medicine in 2012 (16) and 2013 (17).^{35}Cl MR imaging was conducted with a 7-T whole-body MR system (Magnetom 7T; Siemens Healthcare, Erlangen, Germany) by using a double-resonant (^{35}Cl and ^{1}H) high-pass quadrature birdcage coil with 12 rungs, an inner coil diameter of 22 cm, and a length of 23 cm (QED, Mayfield Village, Ohio). The 7-T system and also the ^{35}Cl and ^{1}H coil are operated as investigational devices. However, except for the magnetic field strength, all limits of the International Electrotechnical Commission guideline—including specific absorption rate limits at the ^{35}Cl frequency—are applied in the same manner as for MR imaging at lower magnetic field strengths (18). To compare relaxation times and signal-to-noise ratios (SNRs), ^{23}Na MR imaging was performed by using a double-resonant (^{23}Na and ^{1}H) quadrature birdcage coil with an inner coil diameter of 26 cm (Rapid Biomed, Rimpar, Germany).

Imaging Protocol

All ^{23}Na and ^{35}Cl images were acquired with a three-dimensional (3D) density-adapted–projection reconstruction technique with isotropic spatial resolution (19). This technique samples k-space on radial lines to achieve short echo times (TEs) of less than 1 millisecond. In contrast to conventional 3D radial acquisition techniques, where k-space is sampled with constant gradient amplitude (ie, constant velocity in k-space), the gradient amplitude is reduced in the outer part of k-space to achieve a more homogeneous distribution of the sampling points. This leads to higher SNR and fewer artifacts compared with conventional 3D radial acquisition techniques. Image reconstruction was performed offline (Matlab; MathWorks, Natick, Mass). The acquired k-space data were filtered to reduce Gibbs ringing artifacts by using a Hamming filter. No filter was applied for the phantom SNR measurements (Table 1, sequences a and b). The k-space data were regridded with an oversampling ratio of two to a Cartesian grid by using a Kaiser-Bessel kernel (20), followed by a conventional fast Fourier transform.

Filtering and fast T2* decay lead to a broadening of the full width at half maximum of the point spread function (PSF). Thus, the effective spatial resolution is lower than the nominal spatial resolution. To quantify the additional loss in spatial resolution caused by the fast T2* decay of ^{35}Cl, the PSFs were simulated by using measured ^{35}Cl relaxation times and the applied pulse sequence parameters (Table 1).

Phantom Studies

SNR was determined according to the definition of the National Electrical Manufacturers Association (21). Image noise was determined by using *noise-only* images. SNRs were measured by using a spherical phantom containing 2.6 L of NaCl solution without agar gel (concentration, 154 mmol/L). For comparison of SNR between ^{35}Cl MR imaging and ^{23}Na MR imaging, the sequence parameters (Table 1, sequences a and b, respectively) were chosen in a way that saturation effects could be neglected (TR much greater than T1) and T2* relaxation effects were minimized (TE much less than T2*).

The NaCl solutions (concentration, 154 mmol/L) containing different agar gel concentrations (0%, 1%, 2%, 3%, 4%, 5%) were examined to compare ^{23}Na and ^{35}Cl relaxation times. For the preparation of the phantoms, agar (Carl Roth, Karlsruhe, Germany) was dissolved in the NaCl solution and heated up to 90°C with stirring. For all measurements, NaCl with natural abundances of ^{23}Na (100%) and ^{35}Cl (75.8%) were used (ie, 154 mmol/L NaCl contains 117 mmol/L ^{35}Cl). To determine T1, 31 ^{35}Cl and 23 ^{23}Na 3D density-adapted–projection reconstruction inversion-recovery (IR) sequences with different inversion times (TIs) were applied (TI for ^{35}Cl, 1–12, 14, 16, 18, 20, 22, 24, 26, 28, 30, 35, 40, 45, 50, 60, 70, 80, 90, 100, and 150 milliseconds;

TI for ^{23}Na, 1, 5, 10, 15, 20, 25, 30, 35, 40, 45, 50, 60, 70, 80, 90, 100, 120, 140, 160, 180, 200, 250, and 300 milliseconds [Table 1, sequences c and d, respectively]). To determine T2*, seven 3D density-adapted–projection reconstruction multiecho sequences were applied with different TEs (TE$_1$, 0.3 and 1–6 milliseconds; TE$_2$, 7–13 milliseconds; TE$_3$, 14–20 milliseconds; TE$_4$, 21–27 milliseconds; TE$_5$, 28–34 milliseconds; TE$_6$, 35–41 milliseconds; TE$_7$, 42–48 milliseconds; TE$_8$, 49–55 milliseconds). A flip angle of 90° was used. Additional parameters can be found in Table 1 (sequences e and f).

In Vivo Studies (Human Brain)

To optimize imaging parameters and to correct for relaxation effects, T1 and T2* were measured. Three healthy volunteers were examined to determine T1 and three healthy volunteers were examined to determine T2* of brain tissue. Ten 3D density-adapted–projection reconstruction IR sequences (TI of 3, 6, 9, 12, 15, 20, 25, 30, 40, 50 milliseconds) and 13 3D density-adapted–projection reconstruction double-echo sequences (TE$_1$ of 0.55, 0.75, 1.0, 1.25, 1.5, 1.75, 2.0, 2.5, 3.0, 3.5, 4.0, 5.0, 6.0 milliseconds; TE$_2$ of 7.0, 7.2, 7.5, 7.7, 8.0, 8.2, 8.5, 9.0, 9.5, 10.0–13.0 milliseconds; TE pairs, 0.55 and 7.0 milliseconds; 0.75 and 7.2 milliseconds, and so on) were applied to measure T1 and T2*, respectively. Additional parameters can be found in Table 1 (sequences g and h). Images in the healthy human brain and in two patients with glioblastoma multiforme were acquired. A short delay (100 microseconds) between excitation pulse and signal acquisition, as well as a long TR (TR, 65 milliseconds much greater than T1), was used to achieve minimized relaxation weighting (^{35}Cl MR imaging [Table 1, sequence i]). A second echo (TE, 14 milliseconds) was acquired to calculate a weighted subtraction image with suppressed cerebrospinal fluid (CSF) signal intensity (^{35}Cl subtraction MR imaging) (Fig E1 [online]). To suppress the signal intensity from Cl$^-$ with T1, such as in CSF, an IR sequence was applied (^{35}Cl

Table 1

Parameters of the ^{35}Cl and ^{23}Na MR Imaging Measurements

Imaging Sequence	TR/TE (msec)	Flip Angle (Degrees)	Readout (msec)	Strength (mT/m)	Length (msec)	No. of Data	No. of Radial Projections	Resolution (mm³)/PSF Broadening (%)	FOV	Acquisition Time (min)
a, SNR, phantom, ^{35}Cl MR	250/0.6	90	5	10.96	0.7	128	12000	6/…	50 voxels³, 300 mm³	50
b, SNR, phantom, ^{23}Na MR	250/0.6	90	5	4.98	0.5	256	12000	6/…	50 voxels³, 300 mm³	50
c, T1M, phantom, ^{35}Cl MR	500/0.3	90	5	10.02	0.4	128	6000	6/…	50 voxels³, 300 mm³	30
d, T1M, phantom, ^{23}Na MR	300/0.3	90	5	5.79	0.4	256	6000	6/…	50 voxels³, 300 mm³	50
e, T2*M, phantom, ^{35}Cl MR	200/…*	90	5	12.08	0.8	128	8000	5/…	50 voxels³, 250 mm³	26.7
f, T2*M, phantom, ^{23}Na MR	300/…*	90	5	7.00	0.4	256	8000	5/…	50 voxels³, 250 mm³	40
g, T1M, brain, ^{35}Cl MR	150/0.8	90	5	10.58	0.35	168	3000	10/10	64 × 64 x 32 voxels, zero filling/320 mm³	7.5
h, T2*M, brain, ^{35}Cl MR	35/…†	64	5	11.98	0.35	168	6000	8.9/7	80 × 80 x 40 voxels, zero filling/357 mm³	3.5
i, Brain, ^{35}Cl MR	65/0.7, 14	90	10	10.80	0.5	340	9000	6/17	Volunteers: 128 voxels³, zero filling/384 mm³, zoomed to 225 mm²; patients: 50 voxels³/300 mm³ zoomed to 225 mm²	9.75
k, Brain, ^{35}Cl IR MR	150/0.8	90	5	10.58	0.35	168	4000	10/10	30 voxels³/300 mm³ zoomed to 225 mm²	10
l, Brain, ^{23}Na MR	120/0.3, 12	90	10	7.90	0.5	384	5000	3/…	100 voxels³/300 mm³ zoomed to 225 mm²	10
m, Brain, ^{23}Na IR MR	185/0.75	90	10	5.20	0.5	380	3200	4.5/…	75 voxels³/338 mm³ zoomed to 225 mm²	9.87
n, T1M, muscle, ^{35}Cl MR	100/0.6	90	2	12.44	0.35	64	3500	12/10	64 voxels³, zero filling/357 mm³	9.83
o, T2*M, concentration-weighted, muscle ^{35}Cl MR	60/…‡	90	2.5	9.67	0.5	64	5000	11/13	64 voxels³, zero filling/352 mm³ zoomed to 220 × 250 mm²	5
p, Muscle, ^{23}Na MR	160, 93, 93/0.35, 0.35, 1.35	90, 45, 45	10	5.87	0.5	384	4000	4/…	160 voxels³, zero filling/320 mm³ zoomed to 300 × 250 mm²	10.7, 6.2, 6.2

Note.—Acquisition time = total acquisition time, readout = readout duration, FOV = field of view, length = length of trapezoidal part of readout gradient, resolution = nominal spatial resolution, strength = maximum gradient strength, T1M = T1 measurement, T2*M = T2* measurement. The TE is defined from the center of the excitation pulse to the beginning of the signal acquisition. The total acquisition time was determined as the product of the repetition time (TR) and the number of radial projections. The flip angles are only given for the excitation pulses, since all inversion pulses had a flip angle of 180°. The shape of the readout was defined by the readout duration, the maximum gradient strength, and the length of the trapezoidal part of the readout gradient. The gradient shape determines the nominal spatial resolution. Filtering and fast T2* decay lead to a broadening of the full width at half maximum (full width without T2* decay; approximately 2.0 pixels) of the PSF. Thus, the effective spatial resolution was lower than the nominal spatial resolution. To quantify this loss in spatial resolution, the PSF was simulated by using measured T2* relaxation times of ^{35}Cl. For ^{35}Cl MR imaging, higher gradient strengths were required to achieve the same resolution as for ^{23}Na MR imaging, because of lower gyromagnetic ratio of ^{35}Cl (cf, lower resonance frequency of ^{35}Cl). Additional details of the density-adapted–projection reconstruction pulse sequence can be found in Nagel et al (19).

* In milliseconds, $TE_1 = 0.3$, 1–6; $TE_2 = 7$–13; $TE_3 = 14$–20; $TE_4 = 21$–27; $TE_5 = 28$–34; $TE_6 = 35$–41; $TE_7 = 42$–48; $TE_8 = 49$–55.

† In milliseconds, $TE_1 = 0.55$, 0.75, 1.0, 1.25, 1.5, 1.75, 2.0, 2.5, 3.0, 3.5, 4.0, 5.0, 6.0; $TE_2 = 7.0$, 7.2, 7.5, 7.7, 8.0, 8.2, 8.5, 9.0, 9.5, 10.0–13.0; TE pairs = 0.55 and 7.0, 0.75 and 7.2, and so on.

‡ In milliseconds, $TE_1 = 0.35$, 0.55, 0.75, 1.00, 1.25, 1.50, 2.75; $TE_2 = 4.0$, 4.6, 5.2, 6.0, 6.6, 7.3, 8.0; $TE_3 = 8.0$–14.0.

IR MR imaging; TI, 24 milliseconds [Table 1, sequence k]). For reasons of comparison, conventional ^{23}Na MR imaging, ^{23}Na subtraction MR imaging (Table 1, sequence l), and ^{23}Na IR MR imaging (TI, 41 milliseconds [Table 1, sequence m]) were also performed for one patient with glioblastoma. Reference tubes were used for signal intensity normalization, as described in the figure legends. Measured T1 and T2* of NaCl solution and brain tissue were used to calculate a correction factor. The determined signal intensities of brain tissue were multiplied by this correction factor to calculate the Cl$^-$ concentration.

To compare the nonproton data with conventional MR imaging for the patients with glioblastoma, T1-weighted images were acquired for the clinical routine workup by using a 3-T MR system (Magnetom Tim Trio; Siemens Healthcare) before and after administration of a standard dose of 0.1 mmol per kilogram of body weight of gadobutrol (Gadavist; Bayer Health Care, Wayne, NJ) as contrast medium and a T1-weighted contrast material–enhanced 3D magnetization-prepared rapid acquisition with gradient-echo sequence. Parameters were as follows: TR msec/TE msec/TI msec, 1710/4/1100; in-plane resolution, 0.5 × 0.5 mm^2; number of sections, 128; section thickness, 1.3 mm; and total acquisition time, 7 minutes 37 seconds. T2- weighted fluid-attenuated IR imaging was performed with the following parameters: 8500/133/2400; in-plane resolution, 0.9 × 0.9 mm^2; number of sections, 25; section thickness, 5 mm; and total acquisition time, 3 minutes 9 seconds.

Image postprocessing was performed with software (Matlab, Math-Works; FSL, FMRIB Software Library, Oxford, England) (22,23). The 7-T ^{1}H and ^{35}Cl MR imaging, as well as the 7-T ^{1}H and ^{23}Na MR imaging were each performed without a repositioning of the patient. For 7-T ^{1}H MR imaging, a gradient-echo sequence with a nominal spatial resolution of 1.5 × 1.5 mm^2 was used (TR msec/TE msec, 4.4/1.64; number of sections, 144;

section thickness, 1.5 mm; total acquisition time, 2 minutes 3 seconds). Before postprocessing with the FMRIB Software (registration), the 3D data sets were interpolated to a matrix size of 300 × 300 × 300 voxels, by using the linear interpolation algorithm of the "interp3" function of the Matlab software (MathWorks, Natick, Mass). Anatomic 3-T ^{1}H images obtained in the patient with glioblastoma were registered to the 7-T ^{1}H MR imaging data by using a rigid body algorithm with 6 degrees of freedom (FLIRT [24], part of FSL). The obtained registration matrix was then applied to the ^{23}Na and ^{35}Cl data.

In Vivo Studies (Calf Muscle)

Ten IR sequences were applied to determine T1 relaxation times of calf muscle from three healthy volunteers (TI, 3–6, 8, 10, 15, 20, 30, 40 milliseconds [Table 1, sequence n]). To calculate T2* of muscle tissue, seven multiecho sequences were performed in four healthy volunteers (TE$_1$, 0.35, 0.55, 0.75, 1.00, 1.25, 1.50, 2.75 milliseconds; TE$_2$, 4, 4.6, 5.2, 6.0, 6.6, 7.3, 8 milliseconds; TE$_3$, 8–14 milliseconds [Table 1, sequence o]). Notably, data from one healthy volunteer (19-year-old female subject) were omitted, because a reliable fitting could not be achieved because of very short ^{35}Cl relaxation times (Table 2). These multiecho sequences were also used to quantify the Cl$^-$ concentration in muscle tissue of

the three healthy volunteers and the two patients. Signal intensities of both calf muscle tissue and a phantom tube (54 mmol/L NaCl solution and 4% agar gel) were extrapolated to TE of 0 millisecond (by using biexponential fitting according to Equation [3]) to calculate the Cl$^-$ concentration of muscle tissue. In addition, ^{23}Na MR imaging of the calf muscles was performed to compare the Cl$^-$ and Na$^+$ concentrations. To calculate B$_0$- and B$_1$-corrected Na$^+$ concentration maps, three ^{23}Na MR imaging sequences were applied (Table 1, sequence p). For the B$_0$ correction, off-resonance maps were calculated from the second (TE, 0.35 millisecond) and third (TE, 1.35 milliseconds) measurements, and image reconstruction was performed by using the calculated off-resonance values. To correct for B$_1$ inhomogeneities, a B$_1$ field map was calculated from the first (flip angle, 90°) and the second image (flip angle, 45°), as proposed by Insko and Bolinger (25). Furthermore, anatomic gradient-echo images were acquired with the ^{1}H channel of the coils and the following parameters: 6.1/2.04; nominal spatial resolution, 2 × 2 mm^2; number of sections, 192; section thickness, 2 mm; and total acquisition time, 2 minutes 50 seconds. The 7-T ^{1}H and ^{35}Cl MR imaging, as well as 7-T ^{1}H and ^{23}Na MR imaging, were each performed without repositioning the patient. Therefore, no registration was performed.

Table 2

T2* ^{35}Cl Relaxation Times and Cl$^-$ Concentrations of Calf Muscle Tissue

Subject No./Sex/Age (y)	T2*$_f$ (msec)	T2*$_s$ (msec)	A_f (%)	Concentration (mmol/L)
Healthy volunteers				
1/F/43	0.38 ± 0.12	3.7 ± 1.3	73 ± 4	10 ± 2
2/M/73	0.34 ± 0.12	2.3 ± 0.6	62 ± 7	11 ± 2
3/F/48	0.39 ± 0.11	3.0 ± 0.7	73 ± 4	13 ± 2
4/F/19	0.18 ± 0.05*	2.1 ± 0.2	76 ± 7	22 ± 8*
Patients				
1/F/44	0.37 ± 0.10	2.6 ± 0.2	55 ± 5	18 ± 3
2/F/28	0.40 ± 0.09	2.7 ± 0.2	50 ± 3	16 ± 1

Note.—Data are means ± standard deviations.

* The short component T2*$_f$ of the T2* of volunteer 4 might include a substantial systematic error. The calculated relaxation time is much shorter than the shortest TE (TE = 0.35 millisecond). Thus, this value and the resulting calculated concentration might also have a large systematic error. Therefore, the values of volunteer 4 were omitted.

Statistical Analysis

This study was designed to demonstrate feasibility of [35]Cl MR imaging. A small number of healthy volunteers ($n = 14$) and patients ($n = 4$) were examined. The small population did not permit a statistical analysis to compare both groups.

The relaxation times were calculated by using a mono- and a biexponential model for the T1 (Eq [2]) and T2* (Eq [3]), respectively. The signal intensity, SI, was measured as a function of the TI and the TE. Curve fitting was applied with the nonlinear least squares routine (Origin, version 8; OriginLab, Northamptom, Mass).

$$SI_{TI} = \sqrt{M_0^2(1 - 2e^{-TI/T1} + e^{-TR/T1})^2 + N^2} \quad (2)$$

$$SI_{TE} = \sqrt{M_0^2\left[A_f\ e^{-TE/T2^*_f} - (1 - A_f)\ e^{-TE/T2^*_s}\right]^2 + N^2} \quad (3)$$

M_0 denotes the equilibrium magnetization. Image noise (N) was taken into account. The relative fractions of the fast component A_f and the slow component ($A_s = 1 - A_f$) of the T2* were set to $A_f = 0.6$ and $A_s = 0.4$, respectively, for phantom imaging, in accordance with the relaxation theory of spin 3/2 nuclei (26). For in vivo imaging A_f was used as a free parameter. For the individual values, the standard error of the fits is presented. In addition, mean values and standard deviations of all measurements were calculated.

Results

Phantom Studies

The SNR measurement revealed SNRs of 12 ([35]Cl MR imaging) and 179 ([23]Na MR imaging), which leads to an approximately 15-fold lower SNR for [35]Cl MR imaging, compared with [23]Na MR imaging. Thus, the required voxel volumes in [35]Cl MR imaging had to be larger by a factor of approximately 15 than those of [23]Na MR imaging to achieve similar SNR. Acquisition parameters and the phantom solution were selected in a way that the influence of relaxation

Figure 1: T1, T2*$_f$, and T2*$_s$ (T_X) of 154 mmol/L NaCl solution containing different concentrations of agar gel. The signal decay with increasing TEs was fitted biexponentially. [35]Cl exhibits much shorter relaxation times than [23]Na.

time differences to the calculated SNR ratio was negligible.

In pure 154 mmol/L NaCl solution, T1 and T2* were about 40% shorter for [35]Cl than for [23]Na (Fig 1). The differences in [35]Cl and [23]Na relaxation times increased with higher concentrations of agar. Thus, for high agar concentrations, the [35]Cl signal can have more loss due to T2* decay than the [23]Na signal, and the calculated SNR can be larger compared with the idealized situation described above.

In Vivo Studies (Human Brain)

[35]Cl T2* of healthy human brain turned out to be very short (T2*$_f$ = 1.2 milliseconds ± 0.3; T2*$_s$ = 7 milliseconds ± 2; A_f = 41% ± 10; number of healthy volunteers, three). A monoexponential fit of T1 revealed a value of 9.2 milliseconds ± 0.7 ($n = 3$). T1 and T2* were evaluated in regions of interest similar to the region of interest (circle 2) in Figure 2a. Data of the individual volunteers are presented in Tables E1 and E2 (online). In an acquisition time of 10 minutes, an isotropic nominal spatial resolution of 6 mm³ was achieved (Fig 2a). The Cl⁻ concentration of CSF was about 100 mmol/L. In brain tissue, the estimated Cl⁻ concentration was
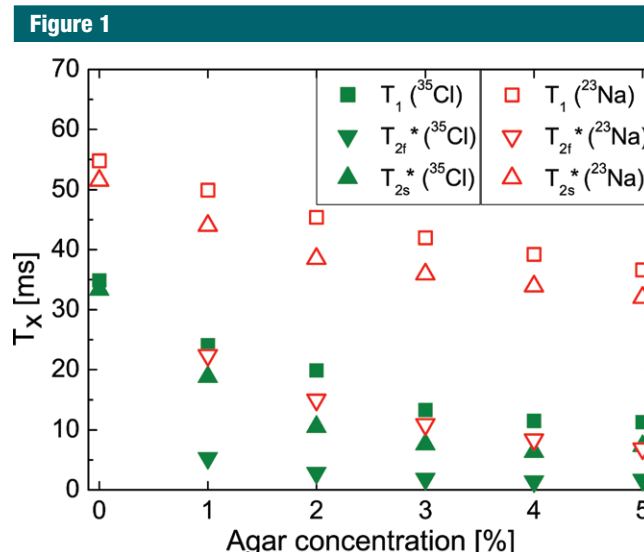
36 mmol/L (Fig 2a). Analogous to IR techniques in [23]Na MR imaging, techniques that suppress signal from extracellular compartments (27–30) and enable a weighting toward intracellular Na⁺ were applied to [35]Cl MR imaging. This way, a fluid suppression could be achieved. The isotropic nominal spatial resolution of [35]Cl IR MR imaging was 10 mm³ (Fig 2b).

To date, only few disorders that feature a changed cytoplasmic Cl⁻ concentration have been described. Malignant brain tumors, especially, glioblastoma multiforme, have in the past shown an elevated Cl⁻ content (31). Therefore, we examined two patients with glioblastoma multiforme. As their [35]Cl MR imaging results were similar (Fig E2 [online]) and [23]Na MR imaging could only be performed in the first patient, we present the images of a 67-year-old female patient (Fig 3). Conventional contrast-enhanced ^{1}H MR imaging demonstrated enhancing parts; and [1]H T2-weighted fluid-attenuated IR MR imaging, the perifocal edema (Fig 3a). Within the affected tissue, concentration-weighted [23]Na and [35]Cl MR imaging revealed increased signal intensities (Fig 3b, 3c, left, respectively). [23]Na

IR MR imaging and ^{35}Cl IR MR imaging showed dissimilar signal intensity behavior. Whereas large parts of the affected brain area exhibited a decreased ^{23}Na IR signal intensity (Fig 3b, middle), the ^{35}Cl IR signal showed approximately a factor of two higher signal intensity than normal brain tissue (Fig 3c, middle). ^{35}Cl subtraction MR imaging (Fig 3c, right) showed qualitatively similar results to ^{35}Cl IR MR imaging but enabled higher spatial resolution.

In Vivo Studies (Calf Muscle)

The ^{35}Cl T2* of healthy muscle tissue turned out to be shorter (T2*$_f$ = 0.37 millisecond ± 0.03, T2*$_s$ = 3.0 milliseconds ± 0.7, A_f = 69% ± 6, n = 3) than in brain tissue. Data of the individual healthy volunteers and the patients are presented in Table E3 (online) and Table 2. The measured Cl$^-$ concentration of normal muscle tissue was 12 mmol/L ± 2 (n = 3). Data of the individual healthy volunteers and the patients are presented in Table 2. ^{23}Na MR imaging revealed a Na$^+$ concentration of 17 mmol/L.

To further examine the clinical potential of ^{35}Cl MR imaging, we examined two patients who had permanent weakness due to a sustained membrane depolarization at presentation. Because this potential reflects Cl$^-$ concentration gradients, an increased cytoplasmic Cl$^-$ concentration is expected. Compared with 12 mmol/L ± 2 of normal muscle (Fig 4a), the Cl$^-$ concentration was increased to 18 mmol/L ± 3 in the muscle affected with periodic paralysis (Fig 4b). The muscle Na$^+$ concentration was markedly increased (Fig 4d) compared with healthy muscle (Fig 4c). The second patient also had increased Cl$^-$ and Na$^+$ concentrations at presentation (Fig E3 [online]).

Discussion

In this study, the feasibility of ^{35}Cl MR imaging measurements in humans was demonstrated. In addition, we were able to noninvasively visualize pathologic changes of the Cl$^-$ distribution in diseased tissue. The total Cl$^-$
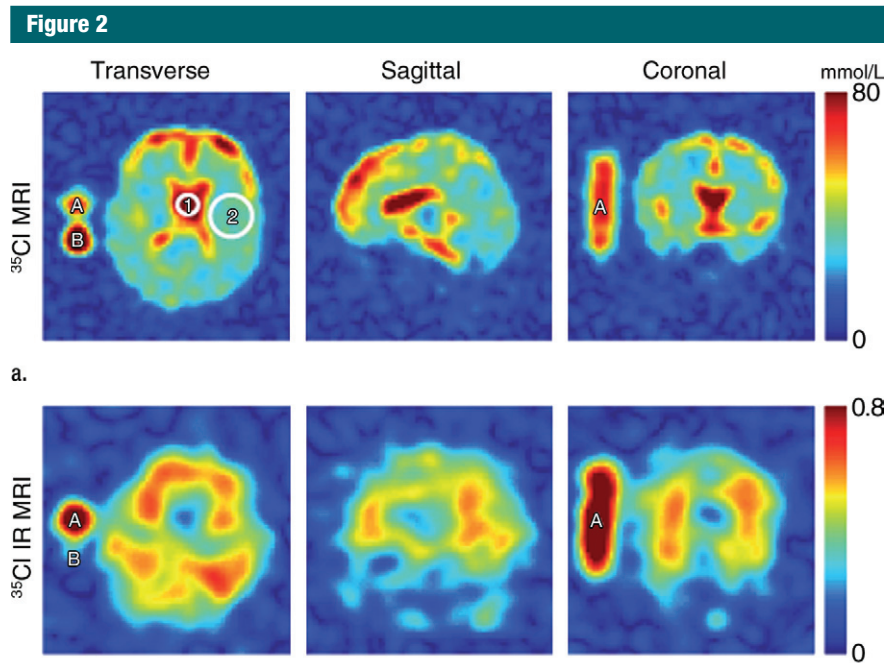

Figure 2: Transverse, sagittal, and coronal sections of a ^{35}Cl MR imaging data set show a healthy human brain in a 67-year-old male subject. Two reference tubes were used (*A*, 103 mmol/L NaCl solution and 4% agar gel; *B*, 103 mmol/L NaCl solution without agar gel). An FOV of 225 × 225 mm^2 is shown. **(a)** Cl$^-$ concentration (^{35}Cl MR imaging) of the total tissue: The signal intensities were measured with a short TE of 0.70 millisecond and a long TR of 65 milliseconds. Normalization was performed with respect to reference tube *B*. Because brain tissue and reference tube *B* have different relaxation properties, the Cl$^-$ concentration of brain tissue is underestimated by a factor of 1.12, when considering the measured relaxation times of brain tissue and saline solution. The Cl$^-$ concentration was determined to be 100 mmol/L in the CSF (circle *1*) and 1.12 · 32 mmol/L = 36 mmol/L in the entire tissue (circle *2*). **(b)** Differences in T1 can be taken advantage of to suppress signal from CSF (^{35}Cl IR MR imaging). Signal intensities were normalized to reference tube *A*. Signal from reference tube *B* is well suppressed in ^{35}Cl IR MR imaging. Color bar = measured Cl$^-$/Na$^+$ concentration in millimoles per liter or measured signal intensity normalized to reference tube *A*.

concentration was estimated with voxel dimensions of 6 mm^3 for brain and 11 mm^3 for skeletal muscle tissue by using 7-T MR imaging. Measurement times for brain and muscle imaging were approximately 10 and 35 minutes, respectively. These would be acceptable for patient examinations in a clinical setting.

The results of our study represent a foray into the noninvasive MR imaging measurement of electrophysiological parameters, such as the resting membrane potential of skeletal muscle cells and the visualization of pathophysiological processes featuring altered Cl$^-$ channels.

Up to now, the total Cl$^-$ concentration in humans in vivo has only been determined with neutron activation analysis

(32). However, this method is nonlocalized, exposes the patient to neutron radiation, and was applied only very rarely. In contrast, ^{35}Cl MR imaging provides a noninvasive and harmless means of investigating Cl$^-$ homeostasis in vivo. We quantified Cl$^-$ concentrations of calf muscle tissue by employing multiecho sequences and biexponential fitting of T2*.

Previously, in vivo ^{35}Cl MR imaging data have only been available at small-animal imaging at 9.4 T (33,34) and 21.1 T (35). Our relaxation time measurements of human brain revealed values that are between the values obtained by Kirsch et al (33) and Schepkin et al (35) in rat brain. We used localized measurements for our study to minimize partial volume effects. However,
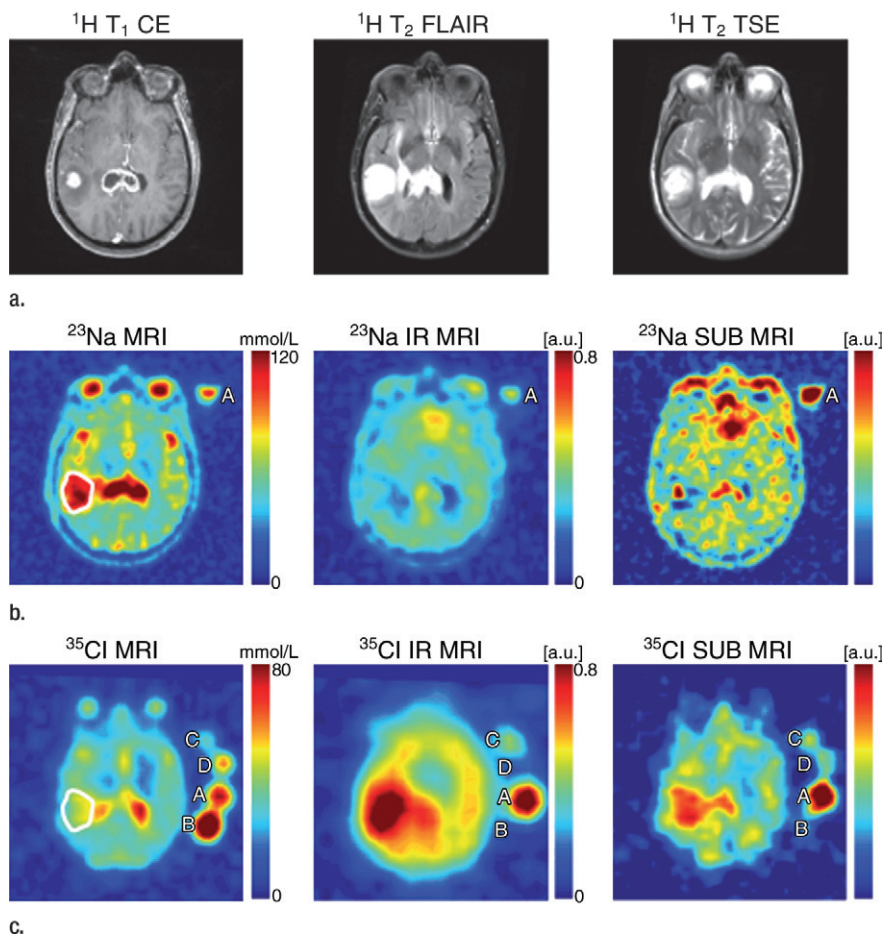
Radiology

Figure 3

Figure 3: Glioblastoma multiforme (WHO grade IV) of the right temporal lobe and the corpus callosum in a 67-year-old female patient. Four reference tubes were used (*A*, 103 mmol/L NaCl solution and 4% agar gel; *B*, 103 mmol/L NaCl solution without agar gel; *C*, 54 mmol/L NaCl solution and 4% agar gel; *D*, 54 mmol/L NaCl solution without agar gel). For ^{23}Na MR imaging, only reference tubes *A* and *B* were used. Signal intensities were normalized to reference tube *B* (^{23}Na and ^{35}Cl MR imaging) and *A* (^{23}Na and ^{35}Cl IR MR imaging and ^{23}Na and ^{35}Cl subtraction MR imaging). **(a)** Contrast-enhanced ^{1}H T1-weighted, ^{1}H T2-weighted fluid-attenuated IR, and ^{1}H T2-weighted turbo spin-echo images show visualization of contrast-enhancing parts and perifocal edema. ^{1}H fluid-attenuated IR and ^{1}H T2-weighted turbo spin-echo images were acquired before contrast agent administration. **(b)** Concentration-weighted ^{23}Na MR imaging revealed elevated signal intensity in all parts of the tumor, whereas ^{23}Na IR MR imaging and ^{23}Na subtraction MR imaging showed parts with reduced and increased signal intensities. **(c)** Slightly increased signal intensities are also visible in ^{35}Cl MR imaging. In contrast to ^{23}Na IR and ^{23}Na subtraction MR imaging, ^{35}Cl IR MR imaging and ^{35}Cl subtraction MR imaging revealed a strong signal increase in the affected brain region. In tumor tissue (white region of interest), a Na$^+$ concentration of 104 mmol/L $\pm$ 10 and a Cl$^-$ concentration of $1.12 \cdot (43$ mmol/L $\pm 6) = 48$ mmol/L ± 7 were measured. Note, the correction factor (of 1.12) was calculated on the basis of healthy brain tissue. The correction factor of tumor tissue might deviate from this value. Signal from reference tubes *B* and *D* is well suppressed in ^{35}Cl IR MR imaging. ^{1}H images were acquired at 3 T; ^{23}Na and ^{35}Cl images, at 7 T. Each ^{23}Na and ^{35}Cl examination required approximately 10 minutes for measurement time. The FOV was 225 $\times$ 225 mm^2. Color bar = measured Cl$^-$/Na$^+$ concentration in millimoles per liter or measured signal intensity normalized to reference tube *A*.

partial volume effects—due to the low spatial resolution—might still have led to a slight contamination of CSF signal in the analyzed region of interest.

In this feasibility study, we observed some limitations that need to be considered for quantitative ^{35}Cl MR imaging. As we demonstrated in the context of muscle imaging, the short ^{35}Cl T2* results in apparent T2* weighting even for common very short–TE imaging techniques (36). Thus, accurate concentration quantification requires a characterization of the relaxation times. In this work, however, no relaxation times of tumor tissue were determined. Therefore, the estimated Cl$^-$ concentrations of tumor tissue might include a systematic error. Relaxation times of healthy brain tissue were applied to calculate the Cl$^-$ concentration. The short T2* also results in an SNR loss. In the context of calf muscle imaging, approximately 50% of the signal has already been decayed at a TE of 0.35 millisecond. In addition, the very short T2* of ^{35}Cl leads to blurring and to a decrease in effective spatial resolution. With the applied parameters, an up to 17% broader full width at half maximum of the PSF was calculated. This calculation results in a corresponding loss in spatial resolution. For clinical application, a breakdown into intra- and extracellular Cl$^-$ concentrations is desirable. However, a direct means of determining distinct values for the intra- and extracellular Cl$^-$ concentrations is not yet available.

For future clinical studies, the physiologically important intracellular Cl$^-$ concentration can be calculated from the total Cl$^-$ concentration, as determined by using ^{35}Cl MR imaging. This calculation could be performed if a two-compartment model and a known extracellular Cl$^-$ concentration—which could easily be determined by analyzing the Cl$^-$ concentration in blood plasma—is assumed. The required values for the intracellular volume fraction are available in the literature (37,38) and can be estimated from ^{23}Na MR imaging measurements (39), as well. The use of literature values for the cell density (37) and the extracellular Cl$^-$ concentration,
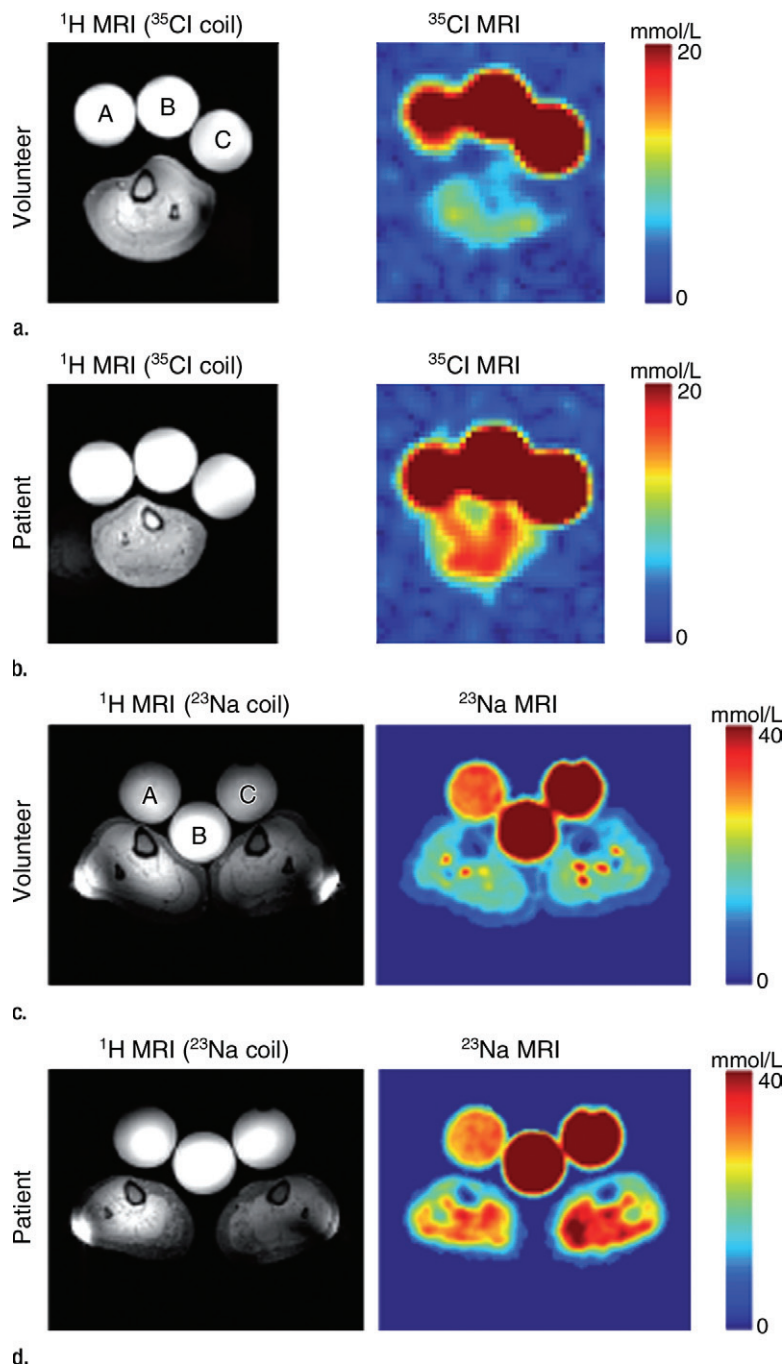
Figure 4

Figure 4: **(a–d)** ^{1}H, ^{35}Cl, and ^{23}Na MR imaging of calf muscles in **(a, c)** a healthy volunteer and **(b, d)** a patient with hypokalemic periodic paralysis. Both individuals were female and were of a similar age (volunteer, 43 years old; patient, 44 years old). ^{1}H MR imaging and ^{35}Cl MR imaging of a single calf were performed with ^{1}H and ^{35}Cl coil (FOV, 220 × 250 mm^2) **(a, b)**. Subsequently, ^{1}H MR imaging and ^{23}Na MR imaging of both calves were performed using ^{1}H and ^{23}Na coil (FOV, 300 × 250 mm^2) **(c, d)**. Note that the ^{1}H MR images show B$_1$-inhomogeneity artifacts that can occur at high-field-strength systems (eg, 7 T) due to the short wavelengths of the ^{1}H resonance frequency. ^{23}Na exhibits an approximately 3.8-fold longer wavelength. Therefore, ^{23}Na images do not show these artifacts. ^{35}Cl MR imaging was conducted with an isotropic nominal resolution of 11 mm^3 in an acquisition time of 5 minutes per data set. The presented image (TE, 0.35 millisecond) already exhibits relaxation (T2*) weighting. Three reference tubes were used (A, 29 mmol/L NaCl and 4% agar gel; B, 54 mmol/L NaCl and 4% agar gel; C, 51 mmol/L NaCl without agar gel). Normalization to the central reference tube B yielded apparent concentrations of 8 mmol/L and 13 mmol/L for the muscle tissue of the volunteer and the patient, respectively. Biexponential fitting—of the signal decays of both reference tube B and muscle tissue—revealed more reliable Cl$^-$ concentrations of 10 mmol/L ± 2 in the volunteer and 18 mmol/L ± 3 in the patient. Sodium concentration maps (nominal spatial resolution = 4 mm^3; total acquisition time, 23 minutes) showed Na$^+$ concentrations of 17 mmol/L (volunteer) and 26 mmol/L (patient). Cl$^-$ and Na$^+$ concentration values were averaged over the calf, whereby the area of the tibia was excluded. The patient's muscle exhibits higher Cl$^-$ and Na$^+$ concentrations than the healthy volunteer's muscle. Color bar = measured Cl$^-$/Na$^+$ concentration in millimoles per liter or measured signal intensity normalized to reference tube A.

together with our results from MR imaging, thus leads to an intracellular Cl$^-$ concentration of 4.0 mmol/L ± 0.8, which is in good agreement with the value obtained from the analysis of biopsy samples (4.1 mmol/L ± 1.5) (40).

In ^{23}Na MR imaging, triple-quantum-filtered imaging (26,41) and IR imaging (27–30) have assisted in skewing the weighting toward intracellular sodium. In our study, ^{35}Cl IR and ^{35}Cl subtraction MR imaging were applied to suppress signal from Cl$^-$ that dilutes extracellular compartments, such as CSF. Larger studies are required to evaluate the putative clinical usefulness of ^{35}Cl IR and ^{35}Cl subtraction MR imaging.

Future clinical ^{35}Cl MR imaging studies might include diseases that feature cellular Cl$^-$ concentration alterations. These include disorders that are caused by altered Cl$^-$ channels. Besides muscular ion channel diseases and tumors, this also includes diseases such as cystic fibrosis (11) and nephronal Cl$^-$ channel diseases (eg, human Bartter syndrome, human X-linked recessive nephrolithiasis) (14).

In the future, imaging techniques that enable even faster signal

acquisition, such as sweep imaging with Fourier transformation, might be used (42,43). Also the application of chlorine 37 (^{37}Cl) may be used to minimize potential T2* weighting. ^{37}Cl exhibits a smaller electrical quadrupole moment than ^{35}Cl (8), which leads to 1.5- to 1.6-fold longer T2*$_f$ (26). As a consequence, ^{37}Cl MR imaging might provide a more accurate quantification of the in vivo Cl$^-$ concentration. However, lower SNR is expected due to the reduced natural abundance (24.22%) (8) and the slightly smaller MR sensitivity of the ^{37}Cl nucleus. Multichannel coils and smaller coils specifically designed for certain areas could further improve image quality and SNR. Once all of the above-mentioned challenges are met, it is likely that a certain level of accuracy will be reached, which will permit solving of the Nernst equation on the basis of MR imaging data. Cell populations' membrane potential could then be estimated with clinically acceptable precision.

In conclusion, our study demonstrates that ^{35}Cl MR imaging examination of humans can be accomplished with a 7-T whole-body MR imaging system within clinically acceptable acquisition times (10–35 minutes) and voxel dimensions of 6 mm³ to 11 mm³, depending on tissue type. In addition, preliminary patient data confirm that pathophysiological changes of the Cl$^-$ homeostasis can be visualized.

Disclosures of Conflicts of Interest: A.M.N. No relevant conflicts of interest to disclose. **F.L.** No relevant conflicts of interest to disclose. **M.A.W.** No relevant conflicts of interest to disclose. **K.J.** Financial activities related to the present article: received a paid scientific award from the Eva Luise Köhler Foundation. Financial activities not related to the present article: none to disclose. Other relationships: none to disclose. **M.B.W.** No relevant conflicts of interest to disclose. **A.R.** No relevant conflicts of interest to disclose. **R.U.** No relevant conflicts of interest to disclose. **W.S.** No relevant conflicts of interest to disclose.

References

1. Hodgkin AL, Katz B. The effect of sodium ions on the electrical activity of giant axon of the squid. J Physiol (Paris) 1949;108(1):37–77.

2. Goldman DE. Potential, impedance, and rectification in membranes. J Gen Physiol 1943;27(1):37–60.

3. Boada FE, LaVerde G, Jungreis C, Nemoto E, Tanase C, Hancu I. Loss of cell ion homeostasis and cell viability in the brain: what sodium MRI can tell us. Curr Top Dev Biol 2005;70:77–101.

4. Ouwerkerk R. Sodium magnetic resonance imaging: from research to clinical use. J Am Coll Radiol 2007;4(10):739–741.

5. Madelin G, Regatte RR. Biomedical applications of sodium MRI in vivo. J Magn Reson Imaging 2013;38(3):511–529.

6. Umathum R, Rösler MB, Nagel AM. In vivo 39K MR imaging of human muscle and brain. Radiology 2013;269(2):569–576.

7. Atkinson IC, Claiborne TC, Thulborn KR. Feasibility of 39-potassium MR imaging of a human brain at 9.4 Tesla. Magn Reson Med Published June 24, 2013. Accessed 2013.

8. Harris RK, Becker ED, Cabral de Menezes SM, Goodfellow R, Granger P. NMR nomenclature: nuclear spin properties and conventions for chemical shifts. IUPAC Recommendations 2001. International Union of Pure and Applied Chemistry. Physical Chemistry Division. Commission on Molecular Structure and Spectroscopy. Magn Reson Chem 2002;40(7):489–505.

9. Koch MC, Steinmeyer K, Lorenz C, et al. The skeletal muscle chloride channel in dominant and recessive human myotonia. Science 1992;257(5071):797–800.

10. Boulenguez P, Liabeuf S, Bos R, et al. Down-regulation of the potassium-chloride cotransporter KCC2 contributes to spasticity after spinal cord injury. Nat Med 2010;16(3):302–307.

11. Jentsch TJ, Stein V, Weinreich F, Zdebik AA. Molecular structure and physiological function of chloride channels. Physiol Rev 2002;82(2):503–568.

12. Cuddapah VA, Sontheimer H. Ion channels and transporters [corrected] in cancer. II. Ion channels and the control of cancer cell migration. Am J Physiol Cell Physiol 2011;301(3):C541–C549.

13. Habela CW, Ernest NJ, Swindall AF, Sontheimer H. Chloride accumulation drives volume dynamics underlying cell proliferation and migration. J Neurophysiol 2009;101(2):750–757.

14. Lehmann-Horn F, Jurkat-Rott K. Voltage-gated ion channels and hereditary disease. Physiol Rev 1999;79(4):1317–1372.

15. Jurkat-Rott K, Weber MA, Fauler M, et al. K+-dependent paradoxical membrane depolarization and Na+ overload, major and reversible contributors to weakness by ion channel leaks. Proc Natl Acad Sci U S A 2009; 106(10):4036–4041.

16. Nagel AM, Meise FM, Weber MA, et al. Chlorine (35Cl) magnetic resonance imaging of the human brain and muscle [abstr]. In: Proceedings of the Twentieth Meeting of the International Society for Magnetic Resonance in Medicine. Berkeley, Calif: International Society for Magnetic Resonance in Medicine, 2012; 1699.

17. Nagel AM, Weber MA, Lehmann-Horn F, et al. Chlorine (35Cl) MRI in humans: Cl$^-$ alterations do not correspond to disease-related Na+ changes [abstr]. In: Proceedings of the Twenty-First Meeting of the International Society for Magnetic Resonance in Medicine. Berkeley, Calif: International Society for Magnetic Resonance in Medicine, 2013; 116.

18. International Electrotechnical Commission. Medical Electrical Equipment. Part 2-33. Particular requirements for the basic safety and essential performance of magnetic resonance equipment for medical diagnosis. IEC 60601-2-33. Geneva, Switzerland: International Electrotechnical Commission, 2010.

19. Nagel AM, Laun FB, Weber MA, Matthies C, Semmler W, Schad LR. Sodium MRI using a density-adapted 3D radial acquisition technique. Magn Reson Med 2009;62(6): 1565–1573.

20. Jackson JI, Meyer CH, Nishimura DG, Macovski A. Selection of a convolution function for Fourier inversion using gridding [computerised tomography application]. IEEE Trans Med Imaging 1991;10(3):473–478.

21. National Electrical Manufacturers Association. Determination of signal-to noise ratio (SNR) in diagnostic magnetic resonace imaging. NEMA Standards Publication M-. Rosslyn, Va: National Electrical Manufacturers Association, 2001.

22. Smith SM, Jenkinson M, Woolrich MW, et al. Advances in functional and structural MR image analysis and implementation as FSL. Neuroimage 2004;23(suppl 1):S208–S219.

23. Woolrich MW, Jbabdi S, Patenaude B, et al. Bayesian analysis of neuroimaging data in FSL. Neuroimage 2009;45(suppl 1):S173–S186.

24. Jenkinson M, Bannister P, Brady M, Smith S. Improved optimization for the robust and

accurate linear registration and motion correction of brain images. Neuroimage 2002; 17(2):825–841.

25. Insko EK, Bolinger L. Mapping of the radio-frequency field. J Magn Reson A 1993;103(1):82–85.

26. Jaccard G, Wimperis S, Bodenhausen G. Multiple-quantum NMR spectroscopy of S=3/2 spins in isotropic phase: a new probe for multiexponential relaxation. J Chem Phys 1986;85:6282.

27. Kline RP, Wu EX, Petrylak DP, et al. Rapid in vivo monitoring of chemotherapeutic response using weighted sodium magnetic resonance imaging. Clin Cancer Res 2000;6(6):2146–2156.

28. Stobbe R, Beaulieu C. In vivo sodium magnetic resonance imaging of the human brain using soft inversion recovery fluid attenuation. Magn Reson Med 2005;54(5):1305–1310.

29. Nagel AM, Amarteifio E, Lehmann-Horn F, et al. 3 Tesla sodium inversion recovery magnetic resonance imaging allows for improved visualization of intracellular sodium content changes in muscular channelopathies. Invest Radiol 2011;46(12):759–766.

30. Nagel AM, Bock M, Hartmann C, et al. The potential of relaxation-weighted sodium magnetic resonance imaging as demonstrated on brain tumors. Invest Radiol 2011;46(9):539–547.

31. Molenaar RJ. Ion channels in glioblastoma. ISRN Neurol 2011;2011:590249.

32. Anderson J, Osborn SB, Tomlinson RW, et al. Neutron-activation analysis in man in vivo: a new technique in medical investigation. Lancet 1964;2(7371):1201–1205.

33. Kirsch S, Augath M, Seiffge D, Schilling L, Schad LR. In vivo chlorine-35, sodium-23 and proton magnetic resonance imaging of the rat brain. NMR Biomed 2010;23(6):592–600.

34. Baier S, Krämer P, Grudzenski S, Fatar M, Kirsch S, Schad LR. Chlorine and sodium chemical shift imaging during acute stroke in a rat model at 9.4 Tesla. MAGMA Published August 10, 2013. Accessed 2013.

35. Schepkin VD, Elumalai M, Kitchen JA, Qian C, Gor'kov PL, Brey WW. In vivo chlorine and sodium MRI of rat brain at 21.1 T. MAGMA Published June 9, 2013. Accessed 2013.

36. Konstandin S, Nagel AM. Measurement techniques for magnetic resonance imaging of fast relaxing nuclei. MAGMA Published July 24, 2013. Accessed 2013.

37. Donahue KM, Weisskoff RM, Parmelee DJ, et al. Dynamic Gd-DTPA enhanced MRI measurement of tissue cell volume fraction. Magn Reson Med 1995;34(3):423–432.

38. Syková E, Nicholson C. Diffusion in brain extracellular space. Physiol Rev 2008;88(4):1277–1340.

39. Thulborn KR, Gindin TS, Davis D, Erb P. Comprehensive MR imaging protocol for stroke management: tissue sodium concentration as a measure of tissue viability in nonhuman primate studies and in clinical studies. Radiology 1999;213(1):156–166.

40. Cunningham JN Jr, Carter NW, Rector FC Jr, Seldin DW. Resting transmembrane potential difference of skeletal muscle in normal subjects and severely ill patients. J Clin Invest 1971;50(1):49–59.

41. Pekar J, Renshaw PF, Leigh JS Jr. Selective detection of intracellular sodium by coherence-transfer NMR. J Magn Reson (1969) 1987;72(1):159–161.

42. Idiyatullin D, Corum C, Park JY, Garwood M. Fast and quiet MRI using a swept radiofrequency. J Magn Reson 2006;181(2):342–349.

43. Idiyatullin D, Suddarth S, Corum CA, Adriany G, Garwood M. Continuous SWIFT. J Magn Reson 2012;220:26–31.